

# Enhanced triboelectricity through visible-light-induced surface charges in BTO-polymer hybrid for coexistence solar-mechanical energy harvesting

Wanheng Lu<sup>a,1</sup>, Xinglong Pan<sup>a,1</sup>, Wei Li Ong<sup>a</sup>, Kaiyang Zeng<sup>b,\*</sup>, Ghim Wei Ho<sup>a,c,\*\*</sup>

<sup>a</sup> Department of Electrical and Computer Engineering, National University of Singapore, 117583, Singapore

<sup>b</sup> Department of Mechanical Engineering, National University of Singapore, 117576, Singapore

<sup>c</sup> Department of Materials Science and Engineering, National University of Singapore, 117575, Singapore

## ARTICLE INFO

### Keywords:

Nanocomposite  
Energy harvesting  
Photoexcitation  
KPFM  
Contact AFM  
EFM

## ABSTRACT

The exploration of hybrid composites holds great promise in the pursuit of synergistic energy-harvesting solutions, providing an efficient approach to tap into multiple energy sources. One striking example is the BTO (BaTiO<sub>3</sub>)-polymer hybrid where its high dielectric constant and the piezo-/ferroelectricity are leveraged to improve the triboelectricity of the polymer-based triboelectric nanogenerator (TENG). Beyond this, the BTO also exhibits a photoactive nature, which, until now, has not been exploited to enhance triboelectricity. In this study, a facile method to exploit BTO's photoresponses in a BTO-polymer hybrid is reported, where surface states present in BTO nanoparticles enable visible spectrum absorption, and the interfaces are designed to facilitate charge spatial separation. Upon visible light illumination, surface charges are generated on the BTO-polymer hybrid, significantly enhancing the photo-induced charge electrification, which in turn boosts the TENG output. These findings demonstrate the possibility of simultaneously harvesting solar and mechanical energies in TENGs using ceramic-polymer hybrids. Additionally, the study employs multiple advanced Scanning Probe Microscopy (SPM) techniques to elucidate the roles of each component and interface in energy harvesting, shedding light on the functional material design. This work not only broadens the variety of energy sources for TENGs but also addresses the growing demand for sustainable and adaptable methods of power generation.

## 1. Introduction

The quest for clean and renewable energy resources to supplant conventional fossil fuels stands as one of humanity's most pressing imperatives. This urgency stems from the escalating severity of environmental pollution, the intensifying specter of global warming, and the deepening crises within our energy landscape [1]. Considerable endeavors are underway to advance technologies that harness energy from natural sources, including solar, bioenergy, thermal energy, mechanical vibration, and more [2]. Among these technologies, the triboelectric nanogenerator (TENG) stands out for its resilience to external environmental factors, such as weather fluctuations, temperature variations, and geographical constraints. The operation of a TENG relies on the synergistic coupling of triboelectricity and electrostatic induction, enabling the conversion of mechanical vibration into electricity [3–7]. The surface charge density of triboelectric materials ( $\sigma'$ ) is a crucial

determinant of TENG performance [3,8], which can be augmented by elevating the dielectric constant of these materials. In the case of polymer-based materials, this enhancement is often achieved by incorporating functional nanomaterials with high dielectric constants, such as metallic gold nanoparticles [9], carbon nanotubes [10], and ceramic particles, into the polymer matrix [11–14]. These studies have demonstrated that establishing a hybrid composite system is a straightforward yet effective approach for enhancing the TENG performance.

Barium titanate (BaTiO<sub>3</sub> or BTO) nanoparticles, a prevalent type of ceramic particle, are frequently introduced into the polymer to create a composite-based TENG, strategically leveraging BTO's high dielectric constant and its ferro-/piezo-electric properties [13,14]. Early investigations into the photorefractive effect [15,16] and photovoltaic effect [17–20] of BTO crystals have highlighted its photoactive nature, wherein charges are generated upon exposure to light. However, research on the impact of light illumination on BTO-polymer-based

\* Corresponding author.

\*\* Corresponding author at: Department of Electrical and Computer Engineering, National University of Singapore, 117583, Singapore.

E-mail addresses: [mpezk@nus.edu.sg](mailto:mpezk@nus.edu.sg) (K. Zeng), [elehgw@nus.edu.sg](mailto:elehgw@nus.edu.sg) (G.W. Ho).

<sup>1</sup> These authors contributed equally to this work.

hybrids remains limited, likely due to BTO's large bandgap (3.2–3.4 eV [21–24]), necessitating ultraviolet (UV) light for activation. Various approaches have been explored to extend light absorption from the UV into the visible region, such as narrowing the bandgap through element doping or inducing oxygen deficiency [25–29]. Essentially, these strategies create surface states (or localized electronic states) near the valence or the conduction band, or both bands, modulating the bandgap [25]. Surface states can serve as shallow centers to generate or trap charges under light illumination, contributing to the photorefractive effect in bulk BTO [30,31] and the photoluminescence of crystalline BTO nanoparticles [32]. Furthermore, engineering the interface between photoactive materials and electrodes can enhance light-to-electricity conversion by optimizing the energy band alignment. This interface engineering enables the photoactive materials/electrode interfaces to act as sinks for photoexcited electrons or holes, facilitating charge separation and reducing charge recombination [33,34]. These advancements indicate that the BTO-polymer hybrid may be tailored to absorb visible light and create a photo-responsive TENG, enabling the simultaneous harvesting of light and mechanical energy.

The pursuit of TENG-based multi-photo-mechanical-energy harvesters traces back to 2013 when the integration of solar cells into a TENG system marked the initial endeavor [35,36]. Recent efforts focus on integrating photoactive narrow bandgap semiconductors into TENG systems, such as organic-inorganic hybrid perovskites like MAPbI<sub>3</sub> [37, 38], inorganic halide perovskites like CsPbBr<sub>3</sub> [39] [40], graphitic carbon nitride (g-C<sub>3</sub>N<sub>4</sub>) [41,42], and bismuth oxyhalide (BiOI) [43]. Using these narrow bandgap materials facilitates the absorption of visible light and the injection of photo-generated charges or carriers into the TENG, thereby achieving a photo-responsive or photo-enhanced TENG. Nevertheless, the utilization of such materials encounters challenges concerning structural stability, material toxicity, synthesis complexity, and also commercial viability. From a practical perspective, it is paramount to develop a robust TENG in a simple, non-toxic, environmentally and economically friendly manner. One such approach involves exploring new functionalities and expanding the applications of conventional materials.

In this study, we investigate the utilization of surface states and interface engineering to enable visible light absorption and light-

induced surface charge generation in the BTO-polymer hybrid, a traditional triboelectric material. The light-induced surface charge injects additional charge to increase the surface charge density of the triboelectric materials when illuminated, thus boosting triboelectricity. This BTO-polymer-based TENG facilitates the concurrent harvesting of solar and mechanical energies within a single device (Fig. 1). To illustrate this concept, we fabricate a model of a BTO-polymer hybrid by incorporating BTO nanoparticles into Poly(methyl)methacrylate (PMMA), a commonly used polymer matrix for various oxide fillers [44]. This BTO-PMMA hybrid is then deposited on a Pt-coated silicon wafer to establish a favorable interfacial alignment, resulting in the final model denoted as BTO-PMMA/Pt. To validate the correlation between the surface charge and light illumination, we employ Kelvin Probe Force Microscopy (KPFM), an advanced scanning probe microscopy (SPM) technique integrated with a light source spanning 400–1100 nm wavelength, for precise surface potential and charge measurements. Contact AFM is complemented with the light source-equipped KPFM to demonstrate the generations of triboelectric charges under light stimulation. Furthermore, a vertical contact/separate TENG is constructed using the BTO-polymer hybrid, and a significant enhancement in the electric output (118 % and 31.7 % increase in voltage and current) is observed upon light illumination. This work showcases the application of the surface states and interface engineering strategies to adapt a conventional ceramic-polymer hybrid, enabling the efficient simultaneous harvesting of the solar and mechanical energy abundant in the environment. Moreover, it is noteworthy that this study utilizes a range of advanced Scanning Probe Microscopy (SPM) techniques for in-situ and interface-/particle-specific investigations. These analyses can elucidate the roles of each component and interface of the hybrid light-induced surface charge generation in energy harvesting and uncover the underlying mechanisms, offering insights into functional material design.

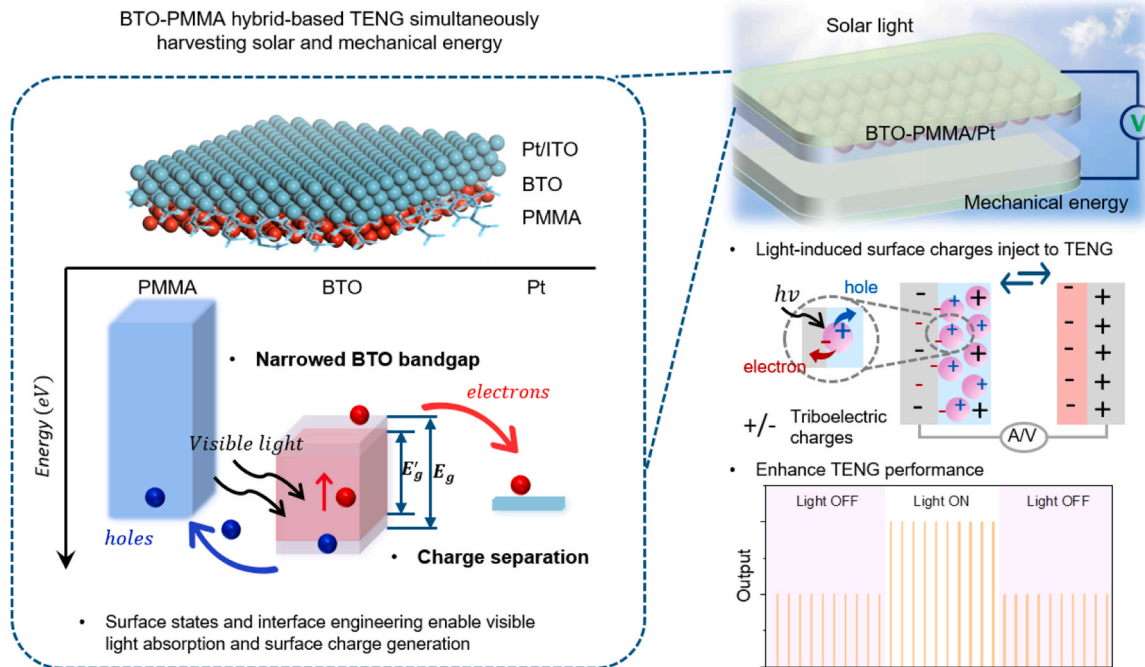


Fig. 1. Schematic of a BTO-PMMA/Pt hybrid-based TENG that can simultaneously harvest mechanical and solar energy.

## 2. Materials and methods

### 2.1. Fabrication of the BTO-PMMA hybrid and the BTO-PMMA-based TENG

Synthesizing BTO nanoparticles: 0.025 mol of Ti-butoxide ( $\text{Ti}[(\text{CH}_2)_3\text{CH}]_4$ , Acros Organics, USA) was diluted with 5 ml of ethanol and 5 ml of deionized water, followed by adding 4 ml of ammonium hydroxide. Furthermore, 0.037 mol of barium hydroxide octahydrate ( $\text{Ba}(\text{OH})_2 \cdot 8\text{H}_2\text{O}$ , Sigma Aldrich, USA) was added to 10 ml of deionized water. Both the mixtures were stirred at  $80^\circ\text{C}$  and later transferred into a 100 ml Teflon-lined stainless steel autoclave with a fill factor of 60 % and then heated to  $200^\circ\text{C}$  for 24 h. Finally, the BTO product was washed with ethanol and deionized water 5 times before being dried at  $80^\circ\text{C}$  for 24 h.

Fabricating BTO-PMMA hybrid: 5 wt% of Poly(methyl) methacrylate (PMMA) was dissolved into sorbitol. 5 or 15 wt% of as-prepared BTO nanoparticles were then mixed into the PMMA solution and stirred at room temperature for 4 h. Subsequently, the mixture was drop cast onto a Pt-coated silicon wafer and dried on a hotplate at  $50^\circ\text{C}$  to form BTO-PMMA/Pt samples. In this work, three sets of control samples, namely (1) PMMA/Pt, (2) BTO/Pt, and (3) BTO-PMMA/Glass were prepared to study the roles of each component and interface in charge generation. To prepare the PMMA/Pt and BTO/Pt samples, pure PMMA solution and pure BTO nanoparticles dispersed in ethanol were deposited on the Pt-coated silicon wafer. To obtain the BTO-PMMA/Glass, the BTO-PMMA mixed solution was dripped on the glass.

Configuring BTO-PMMA-based TENG: A vertical TENG device with a size of  $2 \times 2\text{ cm}^2$  was fabricated, where the top cell was polydimethylsiloxane (PDMS) blade-coated on an indium tin oxide (ITO)-coated glass, and the bottom cell was the BTO-PMMA hybrid blade-coated onto another ITO glass.

### 2.2. Materials characterization

The surface morphology and the chemical components of the samples were analyzed by the scanning electron microscope (SEM) and energy-dispersive X-ray spectroscopy (EDX) (JEOL FEG JSM 7001 F with field-emission operating at 15 kV). The crystalline structure of the prepared BTO nanoparticles was studied by X-ray diffraction (XRD, 5005 Bruker X-ray diffractometer). The chemical structures of the prepared samples were determined by a Fourier transform infrared (FTIR) spectrometer (IR Prestige-21, Shimadzu). The optical absorption spectra (300–1000 nm) were acquired using a UV-Vis-NIR spectrophotometer (UV-3600, Shimadzu). The infrared (IR) images were captured by a thermal imaging infrared camera (E50, FLIR). The open-circuit voltages were recorded by a nanovoltmeter (Keithley 6514).

Four different SPM techniques, including Kelvin Probe Force Microscopy (KPFM), Electrostatic Force Microscopy (EFM), contact Atomic Force Microscopy (contact AFM), and Piezoresponse Force Microscopy (PFM) were employed in this work to measure the surface charge (KPFM & EFM), to create triboelectric charges by rubbing the sample surface (contact AFM) and to determine the polarization state of the sample (PFM). All these SPM measurements were conducted on a commercial SPM system (MPF-3D, Asylum Research, Oxford Instruments, USA) with the conductive Pt-coated silicon tips having a spring constant of 2 N/m and a tip radius of  $\sim 15\text{ nm}$  (AC240, Olympus, Japan). For KPFM and EFM measurements, a double-passing scheme with a lift height of 40 nm was used to minimize the topographic crosstalk. Note that during the first passing, the phase angle was deliberately kept higher than  $90^\circ$  to ensure that the Van der Waal's force between the tip and sample was in the attractive region so that the contact electrification during the first passing could be excluded [45]. For contact AFM, a set point of 1 V corresponding to a force of 100 nN was chosen to ensure good tip-sample contact and also to avoid damage to the sample surface. To examine the effect of the light illumination on the surface charges of the BTO-PMMA

hybrid, the SPM system was integrated with a halogen lamp that offers the full visible spectrum with a wavelength of 400–1100 nm. The wavelength range can be further confined using different optical filters.

## 3. Results and discussion

### 3.1. Structural and chemical analysis

Fig. 2a shows the surface morphology of the PMMA-BTO hybrid with 5 wt% BTO, where particle features can be easily observed, indicating that the BTO nanoparticles are uniformly dispersed in the PMMA matrix. This uniform distribution of BTO in PMMA, also confirmed by the element distribution maps in Fig. 2b and observed in PMMA-BTO hybrid with 15 wt% BTO (Figure S1), ensures that incident light can be effectively transmitted and absorbed by the BTO nanoparticles. Fig. 2c shows the FTIR spectra of the pure PMMA and PMMA-BTO hybrids, where prominent features of pure PMMA spectra are observed, including the C-H stretching ( $2995$  and  $2945\text{ cm}^{-1}$ ), the C=O stretching ( $1717\text{ cm}^{-1}$ ), the C-H bending ( $1431$  and  $1386\text{ cm}^{-1}$ ), the ester group stretching ( $1239$  and  $1144\text{ cm}^{-1}$ ), and the methylene rocking ( $844\text{ cm}^{-1}$ ) [46,47]. Comparing the FTIR spectra of the PMMA-BTO hybrids with that of the pure PMMA, three peaks are observed in the hybrid samples, which belong to the Ti-O-Ti stretching vibrations at  $557\text{ cm}^{-1}$  and two feature bands of  $\text{BaTiO}_3$  at  $1556\text{ cm}^{-1}$  and  $1600\text{ cm}^{-1}$  [48]. When the BTO loading is increased from 5 wt% to 15 wt%, these three feature peaks become sharper. Fig. 2d presents the XRD pattern of the prepared BTO nanoparticles, which matches the diffraction pattern of the tetragonal phase of  $\text{BaTiO}_3$  (JCPDS No. 01-075-0583). Fig. 2e shows the UV-Vis absorption spectra of BTO nanoparticles and the BTO-PMMA hybrid samples with different mass fractions of BTO nanoparticles. All samples exhibit a light absorption cutoff at around 400 nm, indicating the light absorption range has redshifted to the visible light region. Furthermore, the bandgaps of BTO nanoparticles and the hybrids with 5 wt% and 15 wt% BTO are estimated by Tauc Plot (indirect allowed transition,  $(ah\nu)^{1/2}$ ) [49] to be 2.98 eV, 2.86 eV, and 2.88 eV, respectively (the insert of Fig. 2e and Figure S2). These values are smaller than that of bulk BTO (3.2–3.4 eV [21–24]), suggesting visible light absorption in these samples. Given that when a direct allowed transition mode  $((ah\nu)^2)$  is adopted, the bandgaps are estimated to be around 3.2 eV (Figure S2). In this case, the light absorption must blueshift to  $< 387\text{ nm}$ , which contradicts our experimental observations in this work, where the surface charge generation was found under visible light illumination (details will be discussed in the next section). These results, therefore, indicate the presence of localized surface states within the band gap that act as shallow centers to trap/generate charges under light illumination [30–32]. On the other hand, the BTO nanoparticles prepared by hydrothermal methods are also reported to possess a bandgap of less than 3.2 eV, possibly due to the existence of defects in the lattices of BTO nanoparticles [50].

### 3.2. Surface charge generation on BTO-PMMA/Pt hybrid

To study the evolution of the surface charge with light illumination, Kelvin Probe Force Microscopy (KPFM) was integrated with a well-controlled light source with wavelengths ranging from 400 to 1100 nm (Fig. 3a). During the KPFM measurements, the surface potential, strongly associated with surface charge generation, is monitored while varying the illumination conditions. Fig. 3b and c are images of the topography and surface potential of the 15 % BTO-PMMA/Pt hybrid, obtained by KPFM with the light source switched between OFF and ON states. No surface topographic changes are observed in Fig. 3b, indicating that the light illumination does not lead to structural variations on the hybrid surface. However, the surface potential is observed to strongly depend on the light state: a significant increase in the surface potential, around 130 mV, occurs when the light is toggled between ON

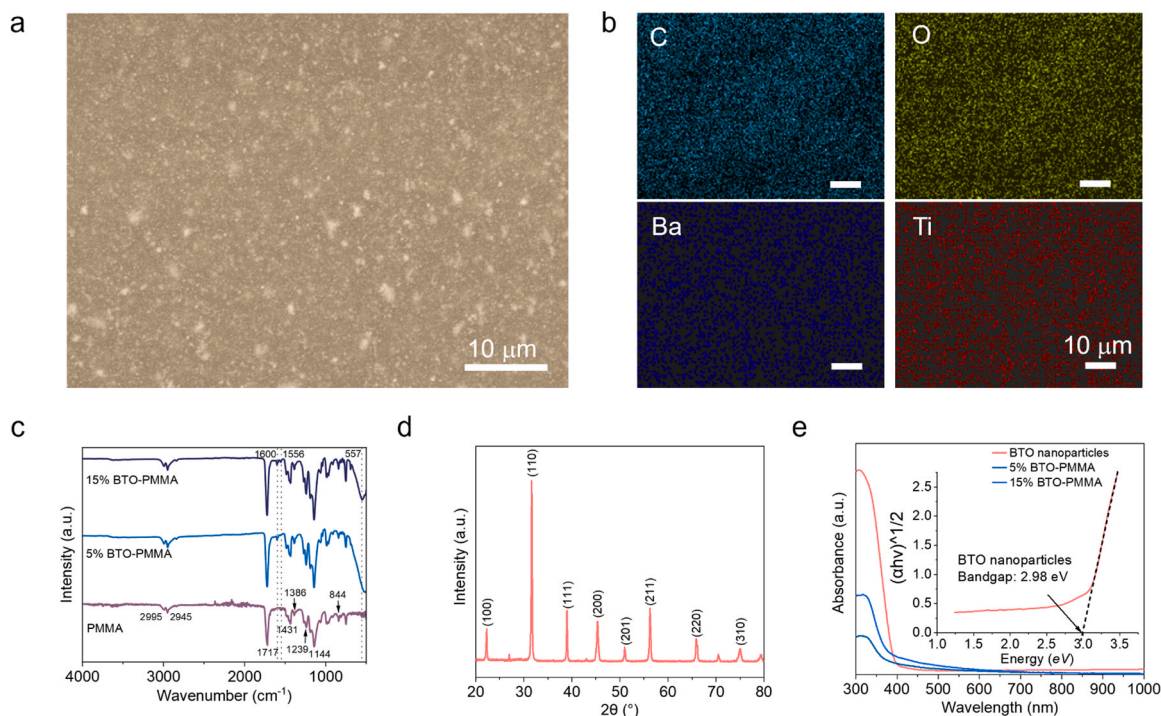


**Fig. 2.** a) SEM image and b) EDX elemental mapping of the 5 % BTO-PMMA/Pt hybrid. c) FTIR spectra of the pure PMMA and the 5 % and 15 % BTO-PMMA hybrids. d) The XRD pattern of the prepared BTO nanoparticles. e) The UV-Vis absorption spectra of BTO nanoparticles, 5 % and 15 % BTO-PMMA hybrid. The insert shows the Tauc Plot of the UV-Vis absorption spectrum of BTO nanoparticles, from which the bandgap of BTO nanoparticles is determined as 2.98 eV.

and OFF (Fig. 3c and Figure S3). This demonstrates that the positive surface charges are generated by the visible light illumination on the BTO-PMMA hybrid.

As discussed in the preceding section, due to the existence of surface states on the BTO nanoparticles (the insert of Fig. 3b and Figure S4 showing BTO nanoparticles with a diameter averaged at around 172 nm), the bandgaps of the BTO nanoparticles and BTO-PMMA hybrids are narrowed, facilitating visible light absorption (Fig. 3d). Thus, BTO nanoparticles play a pivotal role in light absorption and hence surface charge generation. To prove this, the measurements of surface potential with the light ON/OFF, similar to that in Fig. 3b and c, were also conducted on the PMMA/Pt hybrid control sample (Figure S3). Notably, no significant surface potential changes were observed in the PMMA/Pt hybrid, suggesting that the BTO nanoparticles are critical in achieving light-induced surface charge generation. However, this light-induced surface potential jump was also not observed in both BTO nanoparticles dispersed on the Pt-coated substrate and BTO film grown on a Pt-coated silicon wafer (Fig. 3f, g, h, S3, S5). This suggests that besides the visible light absorption enabled by BTO nanoparticles, another essential factor contributes to surface charge generation in the BTO-PMMA/Pt hybrid: the energy band alignment at the interface.

The valence band maximum (VBM) and conduction band minimum (CBM) for BTO are reported to be  $-7.05$  and  $-3.82$  eV (corresponding to a bandgap of 3.23 eV), respectively [51]. For PMMA with a bandgap of  $-5.6$  eV, the lowest unoccupied molecular orbital (LUMO) level is about  $-0.5$  eV, while the highest occupied molecular orbital (HOMO) is  $-6.1$  eV [52]. The work function of the Pt substrate is  $-5.65$  eV [53]. Thus, as depicted in Fig. 3e, this leads to a favorable alignment of the energy bands between the VBM of BTO and the HOMO of PMMA, as well as between the CBM of BTO and Pt. This energy band alignment allows PMMA and Pt to serve as sinks for the photoexcited holes and electrons, respectively. This interface alignment facilitates the spatial separation of the photogenerated charges, effectively minimizing the recombination of holes and electrons. Upon light illumination, BTO first absorbs the light and generates electron-hole pairs. Subsequently, due to the

interface alignment, electrons tend to migrate toward Pt while holes relocate to PMMA. As the KPFM tips scan across the hybrid surface and make contact with the PMMA-BTO hybrid, a surface potential rise or positive surface charge generation is detected when the light is ON. When the light is OFF, the photoexcitation process is stalled, resulting in a gradual decrease in surface potential. Note that the bandgap of nanoparticle BTO used in this work ( $\sim 2.98$  eV) remains consistent with the energy bands in Fig. 3e. To delve deeper into the role of interface alignment in surface charge generation, the surface potential evolutions with light switching were measured on two control samples, namely the BTO/Pt and BTO-PMMA/Glass. In these two samples, only one of two interfaces in the BTO-PMMA/Pt hybrid is present: the interface between the hole sink (PMMA) and photoactive BTO nanoparticles is absent in the BTO/Pt, while that between the electron sink and BTO is non-existent in the BTO-PMMA/Glass. The results presented in Fig. 3f–i, S5, and S6, clearly demonstrate that surface charge generation does not occur in the two control samples, unlike the BTO-PMMA/Pt hybrid. This implies that surface charge generation requires the coupling effect of two interfaces between BTO/PMMA and BTO/Pt and the absence of either interface results in the inability to generate charges under light illumination. More specifically, when exposed to light illumination, BTO nanoparticles absorb the incident photons and generate electron-hole pairs. By virtue of the energy band alignment between Pt, BTO, and PMMA, the electrons and holes preferentially transfer to the BTO/Pt (the electron sink) and the BTO/PMMA interface (the hole sink), respectively. This directional charge movement can spatially separate the photogenerated charges and effectively eliminate charge recombination, resulting in the surface charges on the BTO/PMMA/Pt hybrid. In two control samples, the absence of the BTO/Pt interface in the BTO-PMMA/Glass means that photogenerated electrons cannot be readily transferred to the electron sink, while the missing BTO/PMMA interface in the BTO/Pt sample blocks the hole transfer. Hence, the photo-excited electron-hole pairs could not be separated spatially. The negative and positive charges will recombine, resulting in a surface that tends to be charge-neutral.

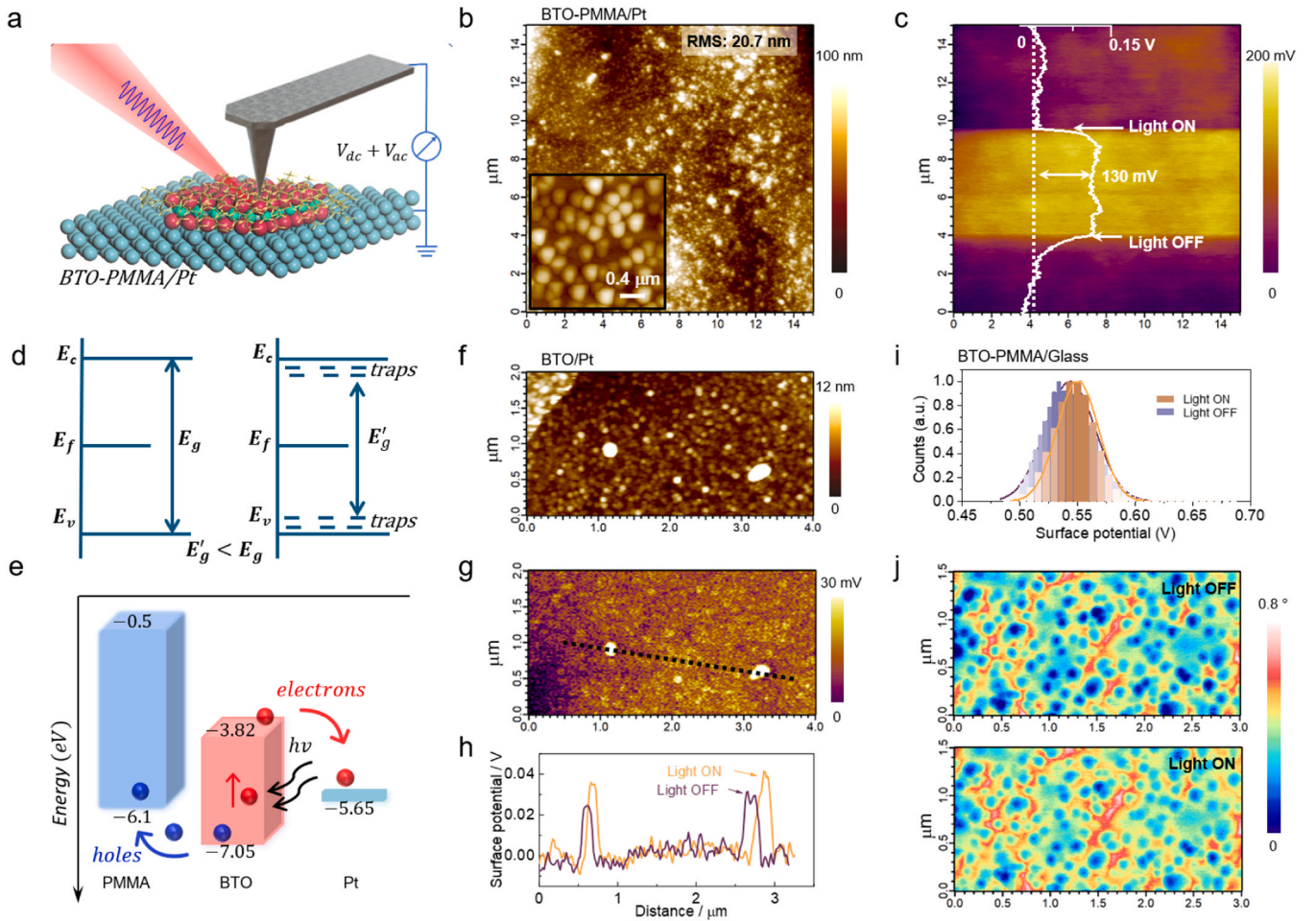


**Fig. 3.** a) Schematic of a light source-attached KPFM for measuring the light-induced surface charge. b) The topography and c) surface potential of the BTO-PMMA/Pt hybrid with light ON and OFF. The insert of Fig. 3b is the topography with a larger magnification. d) Schematic showing that the presence of surface states (working as charge traps) can narrow the bandgap and lower the energy of the incident light required for photoexcitation. e) Schematic showing a favorable alignment of the energy bands between BTO, PMMA, and the Pt substrate. f) The topography, g) the surface potential map (under light), and h) the surface potential profiles (under dark and light) along the dashed line in Fig. 3g of BTO/Pt. i) Histograms of surface potentials of the BTO-PMMA/Glass under dark and light. j) EFM phase images of BTO-PMMA/Pt hybrids under dark and light.

Electrostatic Force Microscopy (EFM), another SPM technique to measure the electrostatic force between the EFM tip and sample is employed to further demonstrate the critical effects of the interfaces on the light-induced surface charge generation. The light-induced surface charge will alter the electrostatic force and this alteration will be reflected in the EMF phase shift [54–56]. Fig. 3j shows the EFM phase shift of the BTO-PMMA hybrid with and without light, where the EFM phase exhibits a positive shift under light illumination, compared with that in the dark. This shift occurs because the attractive electrostatic force between the light-induced positively-charged hybrid surface and a negatively-polarized (-5 V) EFM tip will result in an increase in the EFM phase within the SPM system [54]. Moreover, the phase shifts observed near the BTO/PMMA interface (e.g., featured by a particle morphology) are more pronounced than those without particle-like features (Fig. 3j), and more straightforwardly, the EFM phase shifts around the particles (where the BTO/PMMA interface can be more precisely pinpointed) are found to be more significant (Figure S7). These findings indicate that under light illumination, there is an increased accumulation of positive charges near/at the BTO/PMMA interface, and also underscore the role of the BTO/PMMA interface as a hole sink, responsible for effective electron and hole separation.

### 3.3. Other mechanisms behind the light-induced surface charge generation

Although the mechanisms of the surface states and the interface engineering can well explain the observed surface charge generation upon the visible light illumination (e.g., Fig. 3), other possible mechanisms could contribute to the light-induced surface potential variations. In this section, a series of characterizations were carried out to ascertain the primary mechanisms contributing to the light-induced surface charge generation. One potential factor to consider is that light illumination can cause molecular vibration and heat within the sample, which in turn, can bring about volume change or pyroelectric effects that could alter the surface potential of the BTO-PMMA/Pt hybrid (Fig. 4a). However, the light-induced sample swelling can be excluded according to the surface topography shown in Fig. 3b and S3. The surface topography images and the potential maps were simultaneously acquired, and no surface structural changes were observed with the light switching. Therefore, it can be concluded that surface charge generation is not caused by volume changes.

BTO is a typical pyroelectric material, implying that temperature fluctuations can change the polarization and generate pyroelectric charges, resulting in variations of surface charges (or surface potential) [57]. To discuss the effect of the photo-heating-induced pyroelectricity on the surface potential variations, three key factors need to be considered. First, the temperature fluctuation, rather than temperature

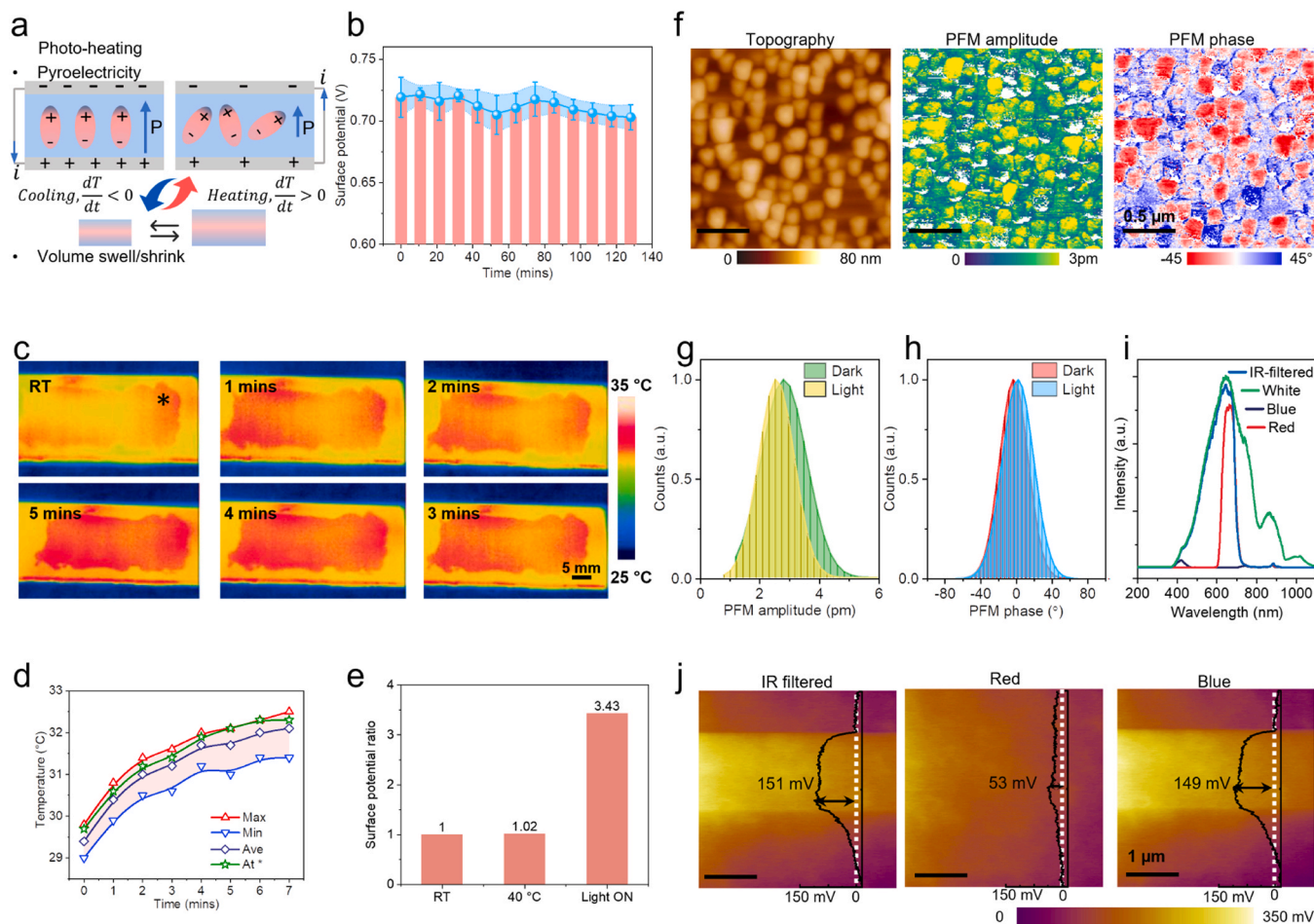


**Fig. 4.** a) Schematic showing the photo-heating effect can also bring about surface potential variation, via e.g., the pyroelectricity generation and volume change. b) Evolution of the surface potential with extended duration of light illumination. c) The infrared images of the BTO-PMMA/Pt hybrid at different exposure durations. d) The temperature evolutions of the BTO-PMMA/Pt hybrid with light illumination including temperature at maximum, minimum, average and point \* marked in Fig. 4c. e) The surface potential ratio against the environment. The surface potential ratio is defined by the surface potential at high temperature or under light illumination to the surface potential at room temperature. f) The topography, PFM amplitude, and PFM phase of the BTO-PMMA/Pt hybrid. The histograms of the g) PFM amplitude and h) PFM phase under dark and light. i) The light spectra of the light source without and with filters. j) The surface potential variations under different optical conditions.

itself, is the prerequisite for the generation of pyroelectric charges. This means that the pyroelectric charges will disappear when the temperature stabilizes [58]. Although the light switching between ON and OFF can produce a short period of temperature fluctuation, the temperature will stabilize when the light is held ON for an extended duration. In the surface potential measurements involving light switching (e.g., Fig. 3c) the light remains ON for 375 seconds and there is no sign of a drop in surface potential. This light-induced surface potential stays consistent and the surface charges persist even when the light exposure duration is extended to around 130 min (Fig. 4b), during which temperature fluctuation is expected to be negligible. In contrast, a remarkable reduction of the pyroelectric charges has been observed in a tourmaline (a typical pyroelectric gemstone) when it reached thermal equilibrium within ~512 seconds [59]. Second, the temperature changes of the BTO-PMMA hybrid induced by the light illumination can be monitored by an infrared camera. As shown in Fig. 4c and d, light illumination causes a temperature increase, but only a 2.6 °C rise and the temperature tends to be stable within 4 mins. When exposed to the light of  $0.2 \text{ W}\cdot\text{m}^{-2}$  (a light intensity similar to those used for KPFM studies), the temperature quickly increases by approximately 2 °C within the first 4 mins and then stabilizes even as the light illumination period increases to 15 mins (Figure S8). A heating/cooling stage was employed to create a temperature fluctuation during KPFM measurements. However, the

temperature fluctuations ( $\Delta T = 3^\circ\text{C}$ ) did not induce any observable surface potential changes on the BTO-PMMA/Pt hybrid. In contrast, surface potential immediately rises once it is illuminated (Figure S9). The huge difference in the effects of temperature and light is further evident in Fig. 4e and S10, where the light illumination leads to a surface potential increase of more than three times, whereas a temperature rise of up to 40 °C only shows a slight effect. Third, the pyroelectric charges are associated with the polarization state of the sample and are negligible when the polarization direction is not well defined [60]. Using Piezoresponse Force Microscopy (PFM) [61], the polarization of the fabricated BTO-PMMA hybrid is found to be random without any preferred polarization state and is unresponsive to light illumination (Fig. 4f–h). This random and light-insensitive polarization of the BTO-PMMA hybrid, along with the independence of surface charges on temperature fluctuation, and the negligible contribution of the temperature to surface potential collectively suggest that the pyroelectric effect is not responsible for surface charge generation observed in the BTO-PMMA/Pt hybrid under light illumination.

The influence of the photo-heating effect on surface charge generation can also be revealed through the examination of surface charge dependence on the intensity and wavelength of the incident light. Higher light intensity and wavelengths extending into the infrared region often promise an enhanced heating effect. As mentioned, the light

source used for SPM measurements in this work can be well controlled with defined intensities and wavelengths by adding various combinations of optical filters (IR and band-pass filters). As shown in Fig. 4i, the light without using any filters covers a full spectrum ranging from 400 to 1100 nm (denoted as white light). Through the use of optical filters, other light conditions were also produced, namely IR-filtered (400 nm to 750 nm), blue light (400 nm to 480 nm), and red light (600 nm to 750 nm). It should be noted that the blue light has an intensity much lower than others. The surface potential variations induced by these different light sources are presented in Fig. 4j, S11, and S12. Notably, the light-induced surface potential variations are almost the same under white, IR-filtered, and blue light, but are much lower under red light. This suggests the negligible effect of the IR light and the light intensity on the surface charge generation. Thus, the photo-heating effect can be ruled out as the mechanism behind the observed light-induced surface charge generation.

### 3.4. Impact of light illumination on triboelectricity

The above results have demonstrated that surface charges can be

generated on the BTO-PMMA hybrid upon the irradiation of visible light. Such a BTO-PMMA hybrid can then be employed in a triboelectric generator (TEG) device. To explore the impact of the visible-light-induced surface charges on the triboelectricity of the BTO-PMMA hybrid, KPFM is combined with contact AFM for in-situ characterization of the triboelectricity at the nanoscale, where the triboelectric charges are created by contact AFM and the surface potential is immediately measured by KPFM [45,62]. Specifically in this work, an area over the BTO-PMMA surface is initially rubbed by the contact AFM tip. Then a larger area encompassing the rubbed area is scanned in the KPFM mode to map the surface potential. The variation in surface potential between the rubbed and the unrubbed area is indicative of the presence of triboelectric charges (Fig. 5a and S13). Fig. 5b and c show the surface potential obtained by this combined contact AFM and KPFM technique with the light ON and OFF, where potentials of the rubbed area are normalized relative to those in the pristine area. The surface potential of the rubbed area is found to be higher when the light is ON, compared to that when the light is OFF, suggesting an increase in the triboelectric charge density under illumination. Note that under both dark and light conditions, positively shifted surface potentials are observed, indicating

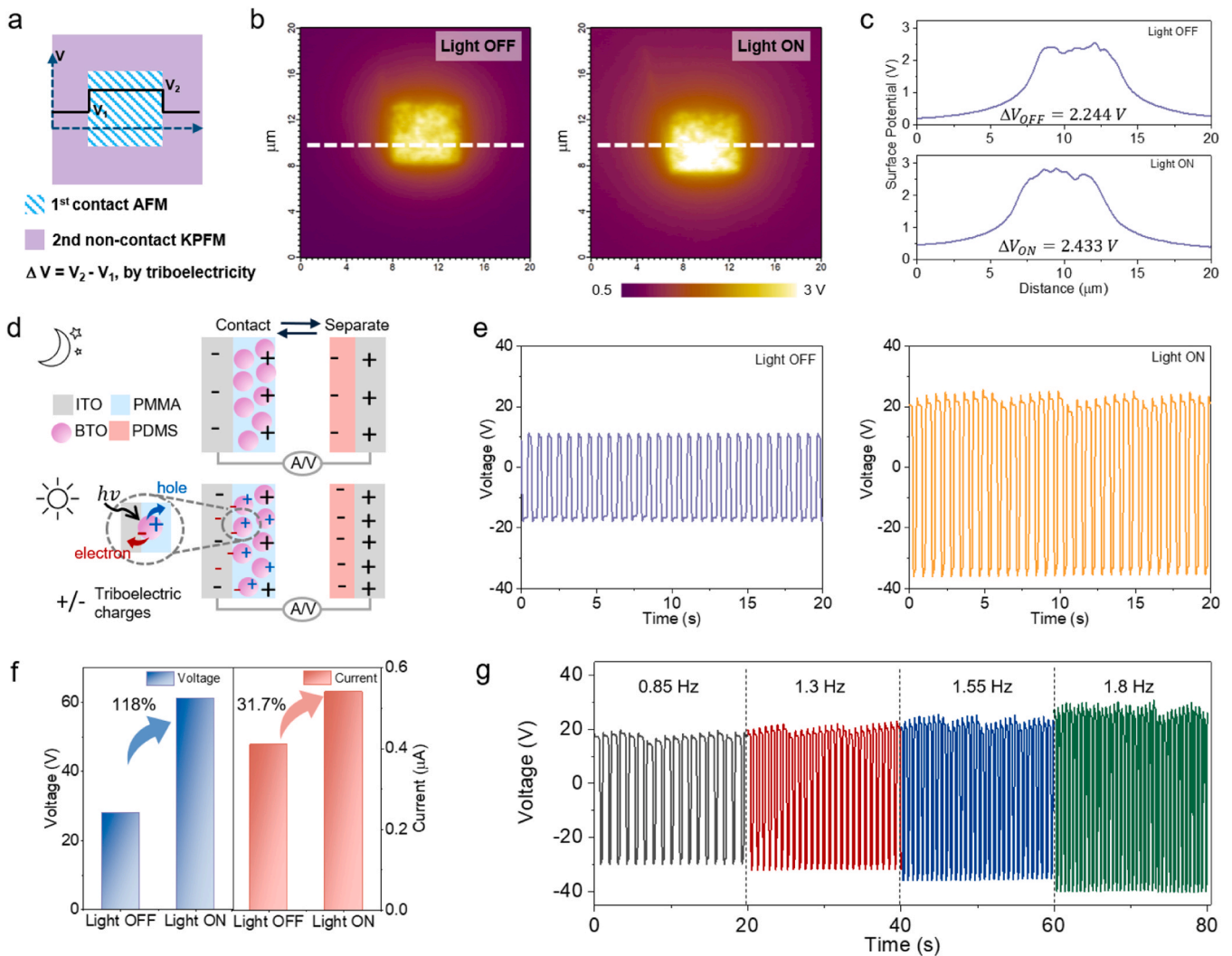


**Fig. 5.** a) Schematic showing the combination of KPFM and contact AFM to study triboelectricity. b) Using the scheme in Fig. 5a, surface potential images were obtained under dark and light. c) The surface potential profiles along the dashed line in Fig. 5b. d) Schematic showing the working mechanisms of a vertical contact/separation TENG based on the BTO-PMMA hybrid in dark and light conditions. Under light illumination, the light-induced surface charges inject to the hybrid surface to increase the total surface triboelectric charge density, thereby enhancing the TENG performance. e) The voltage output from the BTO-PMMA/ITO-based TENG in dark and light conditions. f) Analysis of voltage and current output from the BTO-PMMA/ITO-based TENG in dark and light conditions. g) Frequency dependency of the output voltage of the BTO-PMMA/ITO-based TENG.

that the BTO-PMMA hybrid is the positive triboelectric material relative to Pt. According to the KPFM studies (e.g., Figs. 3c and 4j), positive charges generated by light illumination on the surface of the BTO-PMMA/Pt hybrid, has the same charge polarity as the triboelectric charge on the BTO-PMMA hybrid. Thus, the light-induced increase in triboelectric charge density can be attributed to the additional charge injection by light illumination.

As mentioned, such an increase in the surface charge density of triboelectric materials ( $\sigma'$ ) is a crucial booster for TENG performance [3, 8], thus promising enhanced light-induced performance in the BTO-PMMA hybrid-based TENG. To further validate the augmentation in triboelectric charge density attributed to light exposure at a device level, we fabricated a vertical contact/separation TENG device consisting of a PDMS-coated ITO glass as the moving part, and the BTO-PMMA hybrid-coated ITO as the static part. The TENG device was placed under a solar simulator with the static BTO-PMMA hybrid part facing the light source (Figure S14). In this setup, the Pt-coated silicon wafer was replaced by ITO glass to configure the BTO-PMMA hybrid-based TENG to ensure light transmission through the electrode. ITO has good light transmission in the visible spectrum and also a work function ranging from 4.4 to 4.7 eV [63,64]. Thus, the use of ITO did not change the band energy matching between the interfaces. The actuation of the moving part was controlled by a linear motor to contact the BTO-PMMA hybrid surface with various frequencies and the open-circuit voltage or the short-circuit current of the TENG was measured. In such a vertical TENG of ITO/BTO-PMMA:PDMS/ITO, the PDMS serves as the negative triboelectric layer, while the BTO-PMMA hybrid functions as the positive triboelectric layer [65]. Additionally, the BTO-PMMA hybrid also works as a light absorber as well as a surface charge injector. When the TENG operates in dark conditions, the triboelectric charges generated by the contact/separation between the BTO-PMMA hybrid and PDMS are mainly responsible for the output voltage. In light conditions, BTO absorbs light and generates the electrons and holes. Owing to the energy band alignment between ITO, BTO, and PMMA, the generated electrons and holes have preferred directions or paths to transfer. That is, the negative electrons move to the ITO electrode, and the positive holes are injected into the PMMA to increase the surface charge density, thereby boosting the TENG performance (Fig. 5d).

Fig. 5e and Figure S15 illustrate the voltage and current oscillating with the periodic contact/separation of the TENG under both light ON and OFF conditions. In the absence of light illumination, a peak-to-peak voltage of approximately 28 V and a current of 0.41  $\mu\text{A}$  are recorded. Upon switching on the light of  $1.5 \text{ kW}\cdot\text{m}^{-2}$ , the output rises to around 61 V and 0.54  $\mu\text{A}$ , marking an increase of nearly 118 % in voltage and 31.7 % in current, respectively (Fig. 5f). Under a normal light condition of  $0.8 \text{ kW}\cdot\text{m}^{-2}$ , the output voltage can increase by 37 % to 37 V (Figure S16). This enhancement is notably more significant compared to that achieved in perovskites or bismuth oxyhalide-based TENGs [43,66]. The fabricated BTO-PMMA hybrid-based TENG also exhibits a positive correlation between the output voltage and the oscillation frequency, similar to conventional TENGs [67,68]. As shown in Fig. 5g, the output increases as the oscillation frequency increases. Moreover, the voltage and current of the BTO-PMMA hybrid-based TENG can be stably output under light conditions over around 400 cycles (Figure S17), demonstrating the stability of the fabricated TENG. The electric output is used to charge capacitors and power a calculator for performing calculations (Figure S18). These findings provide empirical evidence of the light enhancement effect on the performance of TENG.

#### 4. Conclusions

In this work, the BTO-PMMA hybrid is used as a model system to study the photoresponsive behaviour of ceramic-polymer hybrids. UV-Vis spectra of BTO-PMMA hybrids and individual BTO nanoparticles confirm the existence of surface states on BTO nanoparticles, which effectively narrowed the bandgap of BTO, enabling photoexcitation

upon visible light illumination. When the BTO-PMMA hybrid is deposited on the electrode that has a work function more negative than the conduction band minimum (CBM) of the BTO, e.g., Pt-coated silicon wafer, it forms a favorable energy band alignment. This alignment designated PMMA and Pt as charge sinks for the photoexcited holes and electrons, respectively. By using multiple Scanning Probe Microscopy (SPM) techniques integrated with a light source, surface charges are found to be generated on the BTO-PMMA-(Pt) hybrid when exposed to visible light illumination, due to the presence of surface states and interface engineering. Moreover, these light-induced surface charges are found to enhance the triboelectric charges and the output voltages of a triboelectric nanogenerator device. Our work highlights the potential of harvesting solar and mechanical energies through the strategic surface states and interface engineering. Note that the hybrid is not limited to the combination of BTO and PMMA, other ceramics or polymers capable of photoexcitation and energy band alignment at interfaces, can similarly achieve the concurrent harvesting of solar and mechanical energies within a single hybrid system.

#### CRediT authorship contribution statement

**Xinglong Pan:** Methodology, Investigation, Data curation. **Wanheng Lu:** Writing – original draft, Methodology, Investigation, Data curation, Conceptualization. **Wei Li Ong:** Writing – review & editing. **Ghim Wei Wei Ho:** Writing – review & editing, Visualization, Supervision, Resources, Project administration, Funding acquisition. **Kaiyang Zeng:** Writing – review & editing, Supervision, Software, Resources, Methodology.

#### Declaration of Competing Interest

The authors declare that they have no known competing financial interests or personal relationships that could have appeared to influence the work reported in this paper.

#### Data Availability

Data will be made available on request.

#### Acknowledgements

This work is supported by the A\*STAR, RIE2025 Manufacturing, Trade and Connectivity (MTC), M22K2c0081. The authors acknowledge the instruction for sample preparation from Dr. Chi Hao Liow and Dr. Xin Lu.

#### Appendix A. Supporting information

Supplementary data associated with this article can be found in the online version at [doi:10.1016/j.nanoen.2024.109867](https://doi.org/10.1016/j.nanoen.2024.109867).

#### References

- [1] D. Ahuja, M. Tatsutani Sustainable energy for developing countries. SAPI EN. S. Surveys and Perspectives Integrating Environment and Society, 2009.
- [2] G. Boyle. Renewable energy. Renewable Energy, by Edited by Godfrey Boyle, pp. 456. Oxford University Press, May 2004. ISBN-10: 0199261784. ISBN-13: 9780199261789. (2004) 456.
- [3] Z.L. Wang, Triboelectric nanogenerators as new energy technology for self-powered systems and as active mechanical and chemical sensors, *ACS Nano* 7 (2013) 9533–9557.
- [4] Z.L. Wang, Towards self-powered nanosystems: From nanogenerators to nanopiezotronics, *Adv. Funct. Mater.* 18 (2008) 3553–3567, <https://doi.org/10.1002/adfm.200800541>.
- [5] Z.L. Wang, G. Zhu, Y. Yang, S. Wang, C. Pan, Progress in nanogenerators for portable electronics, *Mater. Today* 15 (2012) 532–543, [https://doi.org/10.1016/s1369-7021\(13\)70011-7](https://doi.org/10.1016/s1369-7021(13)70011-7).
- [6] S. Wang, L. Lin, Z.L. Wang, Triboelectric nanogenerators as self-powered active sensors, *Nano Eng.* 11 (2015) 436–462, <https://doi.org/10.1016/j.nanoen.2014.10.034>.

- [7] Z. Fang, K.H. Chan, X. Lu, C.F. Tan, G.W. Ho, Surface texturing and dielectric property tuning toward boosting of triboelectric nanogenerator performance, *J. Mater. Chem. A* 6 (2018) 52–57.
- [8] G. Zhu, C. Pan, W. Guo, C.Y. Chen, Y. Zhou, R. Yu, Z.L. Wang, Triboelectric-generator-driven pulse electrodeposition for micropatterning, *Nano Lett.* 12 (2012) 4960–4965.
- [9] J. Chun, J.W. Kim, W.S. Jung, C.Y. Kang, S.W. Kim, Z.L. Wang, J.M. Baik, Mesoporous pores impregnated with Au nanoparticles as effective dielectrics for enhancing triboelectric nanogenerator performance in harsh environments, *Energy Environ. Sci.* 8 (2015) 3006–3012, <https://doi.org/10.1039/c5ee01705j>.
- [10] Y.J. Fan, X.S. Meng, H.Y. Li, S.Y. Kuang, L. Zhang, Y. Wu, Z.L. Wang, G. Zhu, Stretchable porous carbon nanotube-elastomer hybrid nanocomposite for harvesting mechanical energy, *Adv. Mater.* 29 (2017) 1603115.
- [11] J. Chen, H. Guo, X. He, G. Liu, Y. Xi, H. Shi, C. Hu, Enhancing performance of triboelectric nanogenerator by filling high dielectric nanoparticles into sponge PDMS film, *ACS Appl. Mater. Interfaces* 8 (2015) 736–744.
- [12] Y. Yu, Z. Li, Y. Wang, S. Gong, X. Wang, Sequential infiltration synthesis of doped polymer films with tunable electrical properties for efficient triboelectric nanogenerator development, *Adv. Mater.* 27 (2015) 4938–4944.
- [13] G. Suo, Y. Yu, Z. Zhang, S. Wang, P. Zhao, J. Li, X. Wang, Piezoelectric and triboelectric dual effects in mechanical energy harvesting using batio<sub>3</sub>/polydimethylsiloxane composite film, *ACS Appl. Mater. Interfaces* 8 (2016) 34335–34341.
- [14] W. Seung, H.J. Yoon, T.Y. Kim, H. Ryu, J. Kim, J.H. Lee, J.H. Lee, S. Kim, Y.K. Park, Y.J. Park, Boosting power-generating performance of triboelectric nanogenerators via artificial control of ferroelectric polarization and dielectric properties, *Adv. Eng. Mater.* 7 (2017) 1600988.
- [15] Y. Fainman, E. Klancnik, S.H. Lee, Optimal coherent image amplification by two-wave coupling in photorefractive batio<sub>3</sub>, *Opt. Eng.* 25 (1986) 252228.
- [16] K. Buse, Light-induced charge transport processes in photorefractive crystals I: models and experimental methods, *Appl. Phys. B* 64 (1997) 273–291.
- [17] R. Shao, M.P. Nikiforov, D.A. Bonnell, Photoinduced charge dynamics on batio<sub>3</sub> (001) surface characterized by scanning probe microscopy, *Appl. Phys. Lett.* 89 (2006) 112904.
- [18] A. Zenkevich, Y. Matveyev, K. Maksimova, R. Gaynutdinov, A. Tolstikhina, V. Fridkin, Giant bulk photovoltaic effect in thin ferroelectric batio<sub>3</sub> films, *Phys. Rev. B* 90 (2014) 161409.
- [19] V. Fridkin, Ferroelectricity and giant bulk photovoltaic effect in batio<sub>3</sub> films at the nanoscale, *Ferroelectrics* 484 (2015) 1–13.
- [20] S. Zhang, B. Zhang, S. Li, Z. Huang, C. Yang, H. Wang, Enhanced photocatalytic activity in Ag-nanoparticle-dispersed batio<sub>3</sub> composite thin films: Role of charge transfer, *J. Adv. Ceram.* 6 (2017) 1–10.
- [21] K. Suzuki, K. Kijima, Optical band gap of barium titanate nanoparticles prepared by rf-plasma chemical vapor deposition, *Jpn. J. Appl. Phys.* 44 (2005) 2081.
- [22] J. Chen, H. Deng, Y. Pan, D. Zheng, L. Sun, J. Tao, P. Yang, J. Chu, Band gap modulation and improved magnetism of double perovskite Sr<sub>2</sub>K<sub>2</sub>Mo<sub>6</sub> (k = Fe, Co, Ni, Mn) doped batio<sub>3</sub> ceramics, *Ceram. Int.* 48 (2022) 7629–7635.
- [23] M.G. Elmahgary, A.M. Mahran, M. Ganoub, S.O. Abdellatif, Optical investigation and computational modelling of batio<sub>3</sub> for optoelectronic devices applications, *Sci. Rep.* 13 (2023) 4761.
- [24] S. Mukherjee, D. Phuyal, C.U. Segre, S. Das, O. Karis, T. Edvinsson, H. Rensmo, Structure and electronic effects from Mn and Nb co-doping for low band gap batio<sub>3</sub> ferroelectrics, *J. Phys. Chem. C* 125 (2021) 14910–14923.
- [25] H. Tong, S. Ouyang, Y. Bi, N. Umezawa, M. Oshikiri, J. Ye, Nano-photocatalytic materials: possibilities and challenges, *Adv. Mater.* 24 (2012) 229–251.
- [26] J.S. Lee, K.H. You, C.B. Park, Highly photoactive, low bandgap TiO<sub>2</sub> nanoparticles wrapped by graphene, *Adv. Mater.* 24 (2012) 1084–1088.
- [27] M. Pelaez, N.T. Nolan, S.C. Pillai, M.K. Seery, P. Falaras, A.G. Kontos, P.S. Dunlop, J.W. Hamilton, J.A. Byrne, K. O'Shea, A review on the visible light active titanium dioxide photocatalysts for environmental applications, *Appl. Catal. B: Environ.* 125 (2012) 331–349.
- [28] M.M. Khan, S.A. Ansari, D. Pradhan, M.O. Ansari, J. Lee, M.H. Cho, Band gap engineered TiO<sub>2</sub> nanoparticles for visible light induced photoelectrochemical and photocatalytic studies, *J. Mater. Chem. A* 2 (2014) 637–644.
- [29] J. Wang, Z. Wang, B. Huang, Y. Ma, Y. Liu, X. Qin, X. Zhang, Y. Dai, Oxygen vacancy induced band-gap narrowing and enhanced visible light photocatalytic activity of ZnO, *ACS Appl. Mater. Interfaces* 4 (2012) 4024–4030.
- [30] L. Holtmann, M. Unland, E. Krätzig, G. Godefroy, Conductivity and light-induced absorption in batio<sub>3</sub>, *Appl. Phys. A* 51 (1990) 13–17.
- [31] K. Buse, T. Bierwirth, Dynamics of light-induced absorption in batio<sub>3</sub> and application for intensity stabilization, *JOSA B* 12 (1995) 629–637.
- [32] M. Moreira, G. Mambriani, D. Volanti, E. Leite, M. Orlandi, P. Pizani, V. R. Mastelaro, C. Paiva-Santos, E. Longo, J.A. Varela, Hydrothermal microwave: a new route to obtain photoluminescent crystalline batio<sub>3</sub> nanoparticles, *Chem. Mater.* 20 (2008) 5381–5387.
- [33] Q. Wang, Q. Dong, T. Li, A. Gruverman, J. Huang, Thin insulating tunneling contacts for efficient and water-resistant perovskite solar cells, *Adv. Mater.* 28 (2016) 6734–6739.
- [34] H. Zhou, Q. Chen, G. Li, S. Luo, T. Song, H.S. Duan, Z. Hong, J. You, Y. Liu, Y. Yang, Interface engineering of highly efficient perovskite solar cells, *Science* 345 (2014) 542–546.
- [35] H. Guo, X. He, J. Zhong, Q. Zhong, Q. Leng, C. Hu, J. Chen, L. Tian, Y. Xi, J. Zhou, A nanogenerator for harvesting airflow energy and light energy, *J. Mater. Chem. A* 2 (2014) 2079–2087.
- [36] Y. Yang, H. Zhang, Y. Liu, Z.-H. Lin, S. Lee, Z. Lin, C.P. Wong, Z.L. Wang, Silicon-based hybrid energy cell for self-powered electrodegradation and personal electronics, *ACS Nano* 7 (2013) 2808–2813.
- [37] M. Kim, S. Lee, V.A. Cao, M.C. Kim, J. Nah, Performance enhancement of triboelectric nanogenerators via photo-generated carriers using a polymer-perovskite composite, *Nano Energy* 112 (2023) 108474.
- [38] L. Su, Z.X. Zhao, H.Y. Li, J. Yuan, Z.L. Wang, G.Z. Cao, G. Zhu, High-performance organolead halide perovskite-based self-powered triboelectric photodetector, *ACS Nano* 9 (2015) 11310–11316.
- [39] M. Wang, J. Duan, X. Yang, Y. Wang, Y. Duan, Q. Tang, Interfacial electric field enhanced charge density for robust triboelectric nanogenerators by tailoring metal/perovskite Schottky junction, *Nano Energy* 73 (2020) 104747.
- [40] Q. Guo, X. Yang, Y. Wang, W. Xu, J. Duan, Q. Tang, Dielectric hole collector toward boosting charge transfer of CsPbBr<sub>3</sub> hybrid nanogenerator by coupling triboelectric and photovoltaic effects, *Adv. Funct. Mater.* 31 (2021) 2101348.
- [41] D. Kumar, D.G. Jeong, D.S. Kong, Y.C. Hu, S. Ko, K.-T. Lee, S. Yoon, J.Y. Park, J. H. Kim, J.H. Jung, Boosted triboelectric output performance in g-C<sub>3</sub>N<sub>4</sub> embedded p (vdf-trfe) composite via a coupling of photocarrier and ferroelectric dipole, *Nano Energy* 122 (2024) 109320.
- [42] X. Chen, Y. Zhao, F. Wang, D. Tong, L. Gao, D. Li, L. Wu, X. Mu, Y. Yang, Boosting output performance of triboelectric nanogenerator via mutual coupling effects enabled photon-carriers and plasmon, *Adv. Sci.* 9 (2022) 2103957.
- [43] Z. Yu, H. Yang, N. Soin, L. Chen, N. Black, K. Xu, P.K. Sharma, C. Tsanos, A. Kumar, J. Luo, Bismuth oxyhalide based photo-enhanced triboelectric nanogenerators, *Nano Energy* 89 (2021) 106419.
- [44] S. Requena, S. Lacouil, Y.M. Strzemechny, Luminescent properties of surface functionalized batio<sub>3</sub> embedded in poly (methyl methacrylate), *Materials* 7 (2014) 471–483.
- [45] S. Li, Y. Zhou, Y. Zi, G. Zhang, Z.L. Wang, Excluding contact electrification in surface potential measurement using kelvin probe force microscopy, *ACS Nano* 10 (2016) 2528–2535.
- [46] S. Sain, D. Ray, A. Mukhopadhyay, S. Sengupta, T. Kar, C.J. Ennis, P.K. Rahman, Synthesis and characterization of PMMA-cellulose nanocomposites by in situ polymerization technique, *J. Appl. Polym. Sci.* 126 (2012) E127–E134.
- [47] S. Ramesh, K.H. Leen, K. Kumutha, A. Arof, FTIR studies of PVC/PMMA blend based polymer electrolytes, *Spectrochim. Acta Part A: Mol. Biomol. Spectrosc.* 66 (2007) 1237–1242.
- [48] M. Reda, S. El-Dek, M. Arman, Improvement of ferroelectric properties via Zr doping in barium titanate nanoparticles, *J. Mater. Sci.: Mater. Electron.* 33 (2022) 16753–16776.
- [49] Ł. Haryński, A. Olejnik, K. Grochowska, K. Siuzdak, A facile method for tauc exponent and corresponding electronic transitions determination in semiconductors directly from UV–vis spectroscopy data, *Opt. Mater.* 127 (2022) 112205.
- [50] Ö. Küçük, S. Teber, İ.C. Kaya, H. Akyıldız, V. Kalem, Photocatalytic activity and dielectric properties of hydrothermally derived tetragonal batio<sub>3</sub> nanoparticles using TiO<sub>2</sub> nanofibers, *J. Alloys Compd.* 765 (2018) 82–91.
- [51] J.I. Fujisawa, T. Eda, M. Hanaya, Comparative study of conduction-band and valence-band edges of TiO<sub>2</sub>, SrTiO<sub>3</sub>, and batio<sub>3</sub> by ionization potential measurements, *Chem. Phys. Lett.* 685 (2017) 23–26.
- [52] D. Yu, R. Liptak, G. Aggarwal, A. Cheng, S. Campbell, Tunneling conduction in dense silicon quantum dot/poly (methyl methacrylate) composites, *Thin Solid Films* 527 (2013) 261–266.
- [53] H.B. Michaelson, The work function of the elements and its periodicity, *J. Appl. Phys.* 48 (1977) 4729–4733.
- [54] N.S. Malvankar, S.E. Yalcin, M.T. Tuominen, D.R. Lovley, Visualization of charge propagation along individual pili proteins using ambient electrostatic force microscopy, *Nat. Nanotechnol.* 9 (2014) 1012.
- [55] S.E. Yalcin, B. Yang, J.A. Labastide, M.D. Barnes, Electrostatic force microscopy and spectral studies of electron attachment to single quantum dots on indium tin oxide substrates, *J. Phys. Chem. C* 116 (2012) 15847–15853.
- [56] S.E. Yalcin, J.A. Labastide, D.L. Sowler, M.D. Barnes, Spectral properties of multiply charged semiconductor quantum dots, *Nano Lett.* 11 (2011) 4425–4430.
- [57] J. Yoo, W. Gao, K. Yoon, Pyroelectric and dielectric bolometer properties of Sr modified batio<sub>3</sub> ceramics, *J. Mater. Sci.* 34 (1999) 5361–5369.
- [58] A. Cuadras, M. Gasulla, V. Ferrari, Thermal energy harvesting through pyroelectricity, *Sens. Actuators A: Phys.* 158 (2010) 132–139.
- [59] C. Martin Olmos, A.Z. Stieg, J.K. Gimzewski, Electrostatic force microscopy as a broadly applicable method for characterizing pyroelectric materials, *Nanotechnology* 23 (2012) 235701.
- [60] J. Groten, M. Zirkel, G. Jakopic, A. Leitner, B. Stadlober, Pyroelectric scanning probe microscopy: a method for local measurement of the pyroelectric effect in ferroelectric thin films, *Phys. Rev. B* 82 (2010) 054112.
- [61] C.H. Liow, X. Lu, C.F. Tan, K.H. Chan, K. Zeng, S. Li, G.W. Ho, Spatially probed plasmonic photothermic nanoheater enhanced hybrid polymeric–metallic PVDF-Ag nanogenerator, *Small* 14 (2018) 1702268.
- [62] Y.S. Zhou, Y. Liu, G. Zhu, Z.-H. Lin, C. Pan, Q. Jing, Z.L. Wang, In situ quantitative study of nanoscale triboelectrification and patterning, *Nano Lett.* 13 (2013) 2771–2776.
- [63] Y. Park, V. Choong, Y. Gao, B. Hsieh, C. Tang, Work function of indium tin oxide transparent conductor measured by photoelectron spectroscopy, *Appl. Phys. Lett.* 68 (1996) 2699–2701.
- [64] N. Balasubramanian, A. Subrahmanyam, Studies on evaporated indium tin oxide (ITO)/silicon junctions and an estimation of its work function, *J. Electrochem. Soc.* 138 (1991) 322–324.

- [65] M. Parvez Mahmud, N. Huda, S.H. Farjana, M. Asadnia, C. Lang, Recent advances in nanogenerator-driven self-powered implantable biomedical devices. *Adv. Energy Mater.* 8 (2018) 1701210.
- [66] Z. Wei, L. Ding, N. Sun, L.-Y. Dang, H.-R. Sun, J.-C. Han, J.-Q. Zhu, G.-G. Wang, Lead-free  $\text{CsBi}_3\text{I}_{10}$  perovskite based photo-enhanced triboelectric nanogenerator, *Nano Energy* 108 (2023) 108209.
- [67] J. Xiong, P. Cui, X. Chen, J. Wang, K. Parida, M.-F. Lin, P.S. Lee, Skin-touch-actuated textile-based triboelectric nanogenerator with black phosphorus for durable biomechanical energy harvesting, *Nat. Commun.* 9 (2018) 4280.
- [68] Y. Hao, J. Huang, S. Liao, D. Chen, Q. Wei, All-electrospun performance-enhanced triboelectric nanogenerator based on the charge-storage process, *J. Mater. Sci.* 57 (2022) 5334–5345.